Ultrafast current and field driven domain-wall dynamics in van der Waals antiferromagnet MnPS3

Ignacio Alliati
QUB
Richard Evans
University of York https://orcid.org/0000-0002-2378-8203
Kostya Novoselov
National University of Singapore
Elton Santos (esantos@ed.ac.uk)
The University of Edinburgh https://orcid.org/0000-0001-6065-5787

Article

Keywords: External Magnetic Fields, Edge Terminations, Armchair Edges, Ultrathin Device Platforms

Posted Date: October 15th, 2020

DOI: https://doi.org/10.21203/rs.3.rs-90731/v1

Ultrafast current and field driven domain-wall dynamics in van der Waals antiferromagnet $MnPS_3$

Ignacio M. Alliati[1], Richard F. L. Evans[2], Kostya S. Novoselov[3,4], & Elton J. G. Santos[5,†]

[1]*School of Mathematics and Physics, Queen's University Belfast, BT7 1NN, UK*

[2]*Department of Physics, The University of York, YO10 5DD, UK*

[3]*Department of Material Science & Engineering, National University of Singapore, Block EA, 9 Engineering Drive 1, 117575, Singapore*

[4]*Chongqing 2D Materials Institute, Liangjiang New Area, Chongqing 400714, China*

[5]*Institute for Condensed Matter Physics and Complex Systems, School of Physics and Astronomy, The University of Edinburgh, EH9 3FD, UK*

[†]*email: esantos@ed.ac.uk*

The discovery of magnetism in two-dimensional (2D) van der Waals (vdW) materials[1–4] has flourished a new endeavour of fundamental problems in magnetism as well as potential applications in computing, sensing and storage technologies[5–10]. Of particular interest are antiferromagnets [11,12], which due to their intrinsic antiferromagnetic exchange coupling show several advantages in relation to ferromagnets such as robustness against external magnetic perturbations. This property is one of the cornerstones of antiferromagnets[13] and implies that information stored in antiferromagnetic domains is invisible to applied magnetic fields preventing it from being erased or manipulated. Here we show that, despite this fundamental understanding, the magnetic domains of recently discovered 2D vdW $MnPS_3$ antiferromagnet[14,15]

can be controlled via external magnetic fields and electric currents. We realize ultrafast domain-wall dynamics with velocities up to $\sim$1500 m s^{-1} and $\sim$3000 m s^{-1} respectively to a broad range of field magnitudes (0.0001$-$22 T) and current densities ($10^8 - 10^{10}$ A cm^{-2}). Both domain wall dynamics are determined by the edge terminations which generated uncompensated spins following the underlying symmetry of the honeycomb structure. We find that edge atoms belonging to different magnetic sublattices function as geometrical constrictions preventing the displacement of the wall, whereas having atoms of the same sublattice at both edges of the material allows for the field-driven domain wall motion which is only limited by the spin-flop transition of the antiferromagnet beyond 25 T. Conversely, electric currents can induce motion of domain walls in most of the edges except those where the two sublattices are present at the borders (e.g. armchair edges). Furthermore, the orientation of the layer relative to the current flow provides an additional degree of freedom for controlling and manipulating magnetic domains in $MnPS_3$. Our results indicate that the implementation of 2D vdW antiferromagnets in real applications requires the engineering of the layer edges which enables an unprecedented functional feature in ultrathin device platforms.

The emergence of magnetism in 2D vdW materials has opened exciting new avenues in the exploration of spin-based applications at the ultimate level of few-atom-thick layers. Remarkable properties including giant tunnelling magnetoresistance[4,16,17] and layer stacking dependent magnetic phase[18,19] have recently been demonstrated. Even though these studies show that rich physical phenomena can be observed in 2D ferromagnets, the dynamics of domain walls which

determine whether such compounds can be effectively implemented in real life device platforms remains elusive. Very few reports have shed some light on the intriguing behaviour of magnetic domains[20,21] and their walls[22] in ferromagnetic layered materials. The scenario is even less clear for 2D antiferromagnets where the antiferromagnetic exchange coupling between spins adds a level of complexity in terms of the manipulation of the magnetic moments by conventional techniques as zero net magnetization is obtained[13]. Indeed, recent measurements using tunnelling magnetoresistance, a common approach for ferromagnetic materials, unveiled that antiferromagnetic correlations persist down to the level of individual monolayers of $MnPS_3$[23]. This result suggests that yet unexplored ingredients at low dimensionality play an important role in the detection and manipulation of the antiferromagnetic order in 2D vdW compounds. Moreover, how domain walls in $MnPS_3$ behave and can be controlled externally in functional devices for practical applications are still open questions.

Here we show that electrical currents and, unexpectedly, magnetic fields can move domain walls in monolayer $MnPS_3$ at low-temperatures achieving fast velocities within the km s^{-1} limit. While bulk antiferromagnetic compounds are insensitive to magnetic fields, the interplay between low-dimensionality and edge-type offers control over domain wall dynamics via an initially unthinkable external parameter. In configurations where the layer terminates with either a zigzag array of Mn atoms or dangling-bonds, the domain walls are controllable via both currents and magnetic fields at a broad range of magnitudes. For configurations where the edge atoms assume an armchair configuration, the domain wall appears pinned and no motion is observed irrespective of the field intensity or current density applied. Our results indicate a rich variety of possibilities

depending on the edge roughness and introduces the layer termination as one of the determinant factors for integration of 2D antiferromagnets in novel domain-wall based applications.

We firstly investigate how magnetic domains are formed in monolayer $MnPS_3$ through simulating the zero-field cooling process for a large square flake of 0.3 μm $\times$ 0.3 μm using atomistic spin dynamics which incorporate atomistic (several Å's) and micromagnetic (μm-level) underlying details (see full set of details in Supplementary Notes $1-6$). The system is thermally equilibrated above the Curie temperature at 80 K and then linearly cooled to 0 K in a simulated time of 4.0 ns as shown in Figure 1 and Supplementary Movies S1-S2. The time evolution of the easy-axis component of the magnetization S_z is used to display the nucleation of the magnetic domains at different temperatures and magnetic fields. While domain walls appeared at zero field with a large extension over the simulation area (Fig. 1**a-e**), an external field can flush out any domains resulting in a homogeneous magnetization after 2 ns (Fig. 1**f-j**). We also observed that some simulations at zero field ended up in the formation of a monodomain throughout the surface. This suggests that antiferromagnetic domains are not intrinsically stable in $MnPS_3$ similarly as in ferromagnetic layered materials, e.g. CrI_3[22]. Indeed, the metastability of the domains prevents the wall profiles from reaching a truly ground-state configuration as they initially appears winded with several nodes at 0 K (Fig. 1**d**), but incidentally evolved to an unwound state (Fig. 1**e**). A close look reveals a continuous rotation of the spins over the extension of the wall pushing the nodes out of the domain wall profile (Supplementary Figure S10 and Supplementary Movie S3). Such interactions between nodes can extend as long as $\sim$95 nm along the wall which is more that two order of magnitudes larger than the thickness (0.8 nm[14]) of the monolayer $MnPS_3$. At longer times, the domain wall

reaches stability and does not show any sudden variations on the spin configurations.

To determine whether the interplay between metastability and the high magnetic anisotropy of $MnPS_3$ could give additional features to the domain walls, we analyse the local behaviour of the spins in the domain wall (Figure 2). We notice that as the spins rotate from one magnetic domain to another they tend to align with the zig-zag crystallographic direction displaying an angle of $\phi = 64.02^{o}$ (Fig. 2**a-b**). The projections of the total magnetization at the wall over the out-of-plane (S_z) and in-plane (S_x, S_y) components show sizeable magnitudes of S_y and S_x as the spins transition from one domain to another despite the easy-axis anisotropy along of S_z (Fig. 2**c-d**). This indicates a domain wall of hybrid characteristics rather than one of Bloch and Néel type (Fig. 2**e-f**). We can extract the domain wall width $\sigma_{x,y,z}$ by fitting the different components of the magnetization (S_x, S_y, S_z) to standard equations[24] of the form:

$$S_j = \frac{1}{\cosh(\pi(j-j_0)/\sigma_j)}, \quad \text{with} \quad j = x,y \tag{1}$$

$$S_z = \tanh(\pi(z-z_0)/\sigma_z) \tag{2}$$

where j_0 and z_0 are the domain wall positions at in-plane and out-of-plane coordinates, respectively. The domain wall widths are within the range of $\sigma_{x,y,z} = 3.40 - 3.50$ nm. Such small widths are commonly observed in permanent magnetic materials[24] due to their exceptionally high magnetic anisotropy such as $Nd_2Fe_{14}B$ (3.9 nm), $SmCo_5$ (2.6 nm), CoPt (4.5 nm) and Mn overlayers on Fe(001) (4.55 nm)[25]. In these systems, magnetic domains are energetically stable after zero-field cooling due to long range dipole interactions which were also checked in our study resulting in no modifications of the results. Therefore, $MnPS_3$ reunites characteristics from soft-magnets

(large area uniform magnetization) and hard-magnets (large magnetic anisotropy, narrow domain walls) within the same material.

An outstanding question raised by these hybrid features is whether the domain walls can be manipulated by electric currents and magnetic fields. It is well known that antiferromagnets are insensitive to external magnetic fields but are rather controllable through currents particularly in high-anisotropy materials[13,26]. However, the low dimensionality together with the underlying symmetry of the honeycomb structure may lead to novel features on the dynamics of domain walls not yet observed in bulk antiferromagnets. To investigate this we simulate the spin-transfer torque induced by spin-polarized currents and the effect of magnetic fields on a large nano-flake of monolayer $MnPS_3$ of dimensions of 300 nm$\times$50 nm (see Supplementary Note 9 for details). The domain wall is initially stabilized from one-atom-thick wall which broadens and develops a profile during the thermalization over a simulation time of 0.5 ns. The system is then allowed to evolve for longer times ($\sim$ 2 ns) to ensure that no changes are observed in the system close to the end of the dynamics.

Surprisingly, both electric currents and magnetic fields are able to induce the motion of domain walls in the antiferromagnetic $MnPS_3$ resulting in a broad range of velocities (Figure 3). For current-induced domain wall motion, wall velocities up to v =3000 m s^{-1} are seen at a maximum current density of $j = 80 \times 10^9$ A cm^{-2} (Fig. 3**a-b**). At such large values of j, we observe primarily two regimes that are characterized by different dependences of v with j. For $j \leq 30\times$ 10^9 A cm^{-2} (Fig. 3**b**) a linear dependence is noticed which can be described by a one-

dimensional model (Supplementary Note 10) as:

$$v = C_c j \tag{3}$$

where $C_c = \frac{\mu_B \sigma}{2\alpha e m_s t_z}\theta_{SH}$, with μ_b the Bohr magneton, σ the domain wall width, θ_{SH} the spin Hall angle, α the Gilbert damping parameter, e the electron charge, m_s the modulus of the magnetization per lattice, and t_z the layer thickness. Eq.3 is consistent with adiabatic spin-transfer mechanisms in thin antiferromagnets[13,26,27] where the conduction electrons from the current transfer angular momentum to the spins of the wall which keeps its coherence through a steady motion (Fig. 3**a** and Supplementary Movie S4). The value of $C_c = 67.11 \times 10^{-13}\ m^3 C^{-1}$ extracted from our simulation data helps to find other parameters not easily accessible in experiments or from theory, e.g. θ_{SH}. The magnitude of θ_{SH} determines the conversion efficiency between charge and spin currents, and it is the figure of merit of any spintronic application. Using the definition of C_c (Supplementary Note 10), we can estimate $\theta_{SH}(\%) = 0.010$ which is comparable to standard heterostructures and antiferromagnets[13] but at a much thinner limit. This suggests $MnPS_3$ as a potential layered compound for power-efficient device platforms. For $j \geq 40\times\ 10^9$ A cm^{-2} the wall velocities tend to saturate to a maximum magnitude near 3000 m s^{-1} (Fig. 3**b**) with a deviation from the linear dependence observed previously (Eq. 3). This intriguing behaviour can be understood in terms of the relativistic kinematics of antiferromagnets[13,28]. As the wall velocities approach the maximum group velocities (v_{g1}, v_{g2}), which sets the maximum speed for spin interactions into the system, relativistic effects in terms of the Lorenz invariance become more predominant. This is due to the finite inertial mass of the antiferromagnetic domain wall which can be decomposed into spin-waves represented through relativistic wave equations[27–29]. We can extend this idea further in a

2D vdW antiferromagnet by examining the variations of several quantities via special relativity concepts. For instance, the variation of the wall velocities versus current densities can be well analysed using:

$$v = C_c j \sqrt{1-(v/v_{g2})^2} \tag{4}$$

where v_{g2} is the maximum spin-wave group velocity at one of the branches of the magnon dispersion (Supplementary Note 12). Eq.4 includes quasi-relativistic corrections[27,29] to the linear dependence recorded at low values of the density (Eq. 3) and can be solved self-consistently in v for each magnitude of j. Strikingly, Eq.4 provides an accurate description of the wall velocity not only at low magnitudes of the density, where relativistic effects are rather small, but also for $j \geq 40\times 10^9$ A cm^{-2}. At such limit, the domain wall width σ and the domain wall mass $\mathrm{M_{DW}}$ also shrinks and expands, respectively, exhibiting effects similar to the Lorentz contraction (Fig. 3**d-e**). These phenomena can be reasoned by (see Supplementary Note 10 for details):

$$\sigma = \sigma_o \sqrt{1-(v/v_{g2})^2} \tag{5}$$

$$\mathrm{M_{DW}} = \frac{2\rho w t_z \pi}{\sigma_o \sqrt{1-(v/v_{g2})^2}} \tag{6}$$

where σ_o is domain wall width at low-velocities ($\sim$3.41 nm), $\rho = \frac{1}{J_{1NN}\gamma^2}$ (with J_{1NN} the exchange parameter for the first nearest-neighbours and γ the gyromagnetic ratio), w is the width of the stripe of the material, and t_z is the layer thickness. There is a sound agreement between the simulation data (Fig. 3**d-e**) and Eqs. 5−6 over a wide range of velocities with minor deviations occurring above 2500 m s^{-1} due to non-linear spin excitations. We found that at such large wall velocities, spin waves or magnons are emitted throughout the layer with frequencies in the terahertz regime (Fig. 3**f-g**). These excitations can be found in the wake of the wall forming simultaneously in front

and behind the wall motion (see Supplementary Movie S5). Analysing the variations of S_z over time at different j (Supplementary Figure S12), we noticed that high currents generated precession of the spins around the easy-axis with their high in-plane projections (S_x, S_y) being transmitted through spin-waves into the system (Fig. 3**f-g**). This is critical at large values of j where the variation of the position of the domain wall with time results in two velocities before and after the magnons start being excited (Supplementary Figure S12). This behaviour is particularly turbulent at longer times as the wall profile can not be defined any more with the appearance of several vortex, antivortex and spin textures at both edges of the layer and inside the flake (Supplementary Movie S6).

To have a deeper understanding of the characteristics of spin excitations on the domain wall dynamics in $MnPS_3$, we have developed an analytical model using linear spin-wave theory[30,31] that accounts on the magnon dispersion $\varepsilon(\mathbf{k})$ and their group velocities $v_g(\mathbf{k}) = \frac{\partial \varepsilon(\mathbf{k})}{\partial \mathbf{k}}$ over the entire Brillouin zone. Supplementary Note 12 provides a full description of the details involved. The maximum spin-wave group velocities (v_{g1}, v_{g2}) that $MnPS_3$ can sustain at different magnon branches (Supplementary Figure S13) are in the range from $v_{g1} = 2323$ m s^{-1} to $v_{g2} = 3421$ m s^{-1} (Fig. 3**b**). These magnitudes correspond to the highest velocities at which spin excitations can propagate in the system and put the lower (v_{g1}) and upper limits (v_{g2}) where magnons participate in the domain-wall dynamics. Indeed, there is a good agreement with the numerically calculated wall-velocities where the spin-waves start being emitted into the sheet ($\sim$2248 m s^{-1}), and the wall saturates to its maximum speed ($\sim$2970 m s^{-1}). The slightly lower values obtained in the simulations relative to v_{g1} and v_{g2} are due to the effect of damping on the propagation of domain

walls due to the emission of spin-waves. A similar feature has been observed in the past in 3D ferromagnetic[32,33] and antiferromagnetic[27,34] compounds but the emergence of such phenomena in a 2D vdW antiferromagnet is unprecedented. Additionally, we can estimate a maximum wave frequency ($f_{max} = \hbar\varepsilon/2\pi$) corresponding to v_{g2} of about 4.03 THz. This value surpasses those measured in the state-of-the-art antiferromagnetic materials such as in MnO[35], NiO[36,37], $DyFeO_3$[38], $HoFeO_3$[39] and heterostructures combining MnF_2 and platinum[40] by several times. This implies that antiferromagnetic domain walls in $MnPS_3$ can be used as a terahertz source of electric signal at the ultimate limit of a few atoms thick layer.

Remarkably, the application of a magnetic field results in a very counter-intuitive behaviour as the domain wall moves with velocities as high as $\sim$1500 m s^{-1} (Fig. 3**h-j** and Supplementary Note 13 for additional discussions). We can fit most of the field-induced domain wall dynamics for $B \leq 20$ T with:

$$v = 86.28\, B \tag{7}$$

with a linear regression coefficient of $R^2 = 9996$. The motion is steady, keeping the wall shape throughout the motion. We observe however that both the domain wall width and the domain wall mass change their magnitudes in opposite trend as that observed in the current-driven domain wall dynamics (Supplementary Figure S15). We attribute this difference to the distinct operation of the external stimulus on the domain wall. In the current driven case, the action is tightly focused at the centre of the wall, where the angular change in neighbouring spins is the largest. For large currents the wall is not able to relax fully leading to relativistic contraction in the wall width. In contrast, the magnetic field acts across the whole wall and tends to strengthen the spin flop (SF) state, which

in turn leads to an increase in the domain wall width with increasing field strength (Supplementary Figure S15**a**). This effect is sufficient to counteract the relativistic effect (which is also present) and leads to a net decrease of the domain wall mass (Supplementary Figure S15**b**). Wider domain walls naturally have lower mass as they are easier to move until SF states are achieved for fields above 22 T. In addition, some curvature is formed as the wall moves with its starting points from the terminations of the sheet parallel to the wall movement (Fig. 3**a, h** and Supplementary Movie 7). The spins around one edge move in advance relative to those at the middle of the system and at the opposite edge creating a curved wall during the motion (see detailed features in Supplementary Movie 8). Such deviation from the planar wall shape has been reported in hetero-interfaces formed by NiFe/FeMn bilayers[41] but not yet in a monolayer of a 2D vdW antiferromagnet. This indicates a direct relation between domain-wall motion and the material geometry via edge roughness similarly as in magnetic wires[42]. A close look unveils that the type of edge plays a pivotal role in the domain wall dynamics induced by both magnetic fields and electric currents. Sheets terminated with edge atoms in zig-zag (ZZ) and dangling-bond (DB) configurations (Fig. 3**h**) in any combination (e.g. ZZ-ZZ, ZZ-DB, DB-DB) are susceptible to be manipulated by currents. Nevertheless, only domain wall in layers with dissimilar edges (e.g. ZZ-DB) can be controlled by magnetic fields. Borders formed by atoms in the armchair (ARM) configuration remain inert irrespective of the stimulus applied (Supplementary Figure S16). Intriguingly, ARM edges under applied currents show a short displacement of the domain wall at earlier stages of the dynamics ($\sim$0.07 ns) but rapidly stabilizes to a constant position at longer times. As the current flows through the wall, the spins feel the torque induced by the spin-polarized electrons but rather than reorient

the spins to follow the current direction, the spins at the wall precess around the easy-axis with no motion of the domain-wall. This mechanism is shown in details in Supplementary Movies S9-S10. The ARM edge in this case works as an effective pinning barrier for domain-wall propagation.

The control of the domain-wall motion in an antiferromagnetic material via magnetic fields opens a new ground in the investigation of the role of edges on 2D magnetic materials. The fundamental ingredient that enables such phenomena is based on the underlying magnetic sublattices (e.g. A or B) composing the honeycomb structure (Fig. 4**a-c**). Despite the border considered, for edge atoms residing at different sublattices the magnetic field induces a torque at each sublattice that mutually compensates each other generating no net displacement of the domain-wall (Supplementary Movie S11). For edge atoms at the same sublattice the effect is additive inducing the translation of the wall. Indeed, we can further confirm this mechanism analysing the spin interactions present in the system on a basis of a generalized XXZ Heisenberg Hamiltonian in the form of:

$$\mathscr{H} = -\sum_{\langle i,j\rangle} J_{ij}\mathbf{S}_i \cdot \mathbf{S}_j - \sum_{\langle i,j\rangle} \lambda_{ij} S_i^z S_j^z - D\sum_i (S_i^z)^2 - \mu_s \sum_i \mathbf{S}_i \cdot \mathbf{B}_i \tag{8}$$

where $J_{i,j}$ is the bilinear exchange interactions between spins $\mathbf{S}_i$ and $\mathbf{S}_j$ at sites i and j, λ_{ij} is the anisotropic exchange, D is the on-site magnetic anisotropy and $\mathbf{B}_i$ is the external magnetic field applied along the easy-axis (e.g. B_z). We only include bilinear exchange terms in Eq. 8 since biquadratic exchange interactions are negligible in $MnPS_3$[43]. We considered pair-wise interactions in $\langle i, j\rangle$ up to the third nearest neighbours ($3NN$) (Supplementary Table S1). All parameters are calculated using strongly correlated density functional theory based on Hubbard-U methods. Supplementary Notes $1-4$ convey the full details of the approaches employed. Eq. 8 is then applied to

calculate the spin interactions into the system taking into account any angular variations θ of the spins induced by the field. We determine the stability of the system before and after the application of B_z distinguishing the atoms away from the domain wall from those at the wall (Fig. 4**d**). Such procedure is instrumental to unveil the influence of the edges on the energetics of the domain-wall dynamics as the atoms at these two spatial regions may respond differently to a magnetic perturbation. In fact, we found that spins that are distanced from the domain-wall (i.e. spin-up for $\theta = 0$, and spin-down for $\theta = 180^{o}$) do not suffer any angular variation with B_z as the layer reached a new ground-state. Nevertheless, for spins at the domain-wall the new ground-state under a finite field ($B_z \neq 0$) is obtained at a value of θ different to that at $B_z = 0$ (Fig. 4**d-f**). This indicates that the wall spins tend to rotate under magnetic fields and the effect is particularly strong for atoms at the edges. The variations in energy $-\Delta E$ show that when the two edges are similar (Fig. 4**e**) two different sublattices will be localized at the borders which will respond likewise generating similar variation of energies. As the atoms at the edges are more uncoordinated relative to those in the bulk of the system, they gain more energy from aligning with B_z which allows the spins to rotate more freely but in opposite direction compensating any displacement of the domain-wall. The scenario is completely different when the atoms at the edges belong to the same sublattice such as in a ZZ-DB layer (Fig. 4**f**). In this case, $-\Delta E$ has a larger variation at the DB edge due to the lesser coordination with neighbouring atoms and consequently less exchange energy. This results in a more prompt rotation of the spins at the DB edge than that at the ZZ edge dragging the wall slightly ahead with the field (Supplementary Movie S8). Even though our analysis has been applied for $MnPS_3$ it should be universal for any antiferromagnetic layered material with a

honeycomb lattice.

One of the main implications for having uncompensated spins at the edges selectively controlling domain-wall motion in 2D vdW antiferromagnets is that depending how the layer is oriented in a device-platform we can have many possibilities to induce domain wall dynamics. By engineering the type of edges in $MnPS_3$ we can either induce a fast domain-wall dynamics through both current and magnetic fields, or no motion whatsoever via geometrical constrictions. Our findings suggest that 2D layered antiferromagnets would not be invisible to common magnetic probes (e.g. tunnelling magneto-resistance[23]) which is normally problematic for materials that hold antiferromagnetic coupling between the spins within the layer. In this case the antiferromagnetic layer can play a more active role in magnetic structures rather than induce exchange bias in an adjacent ferromagnetic layer[13]. With the rapid integration of magnetic layered materials in applications and the discovery of more compounds with similar characteristics, our predictions will open novel grounds in the investigations of edge-mediated 2D antiferromagnetic spintronics

Supplementary Materials

Supplementary Notes 1−15, Supplementary Movies 1−13 and Supplementary Figures 1−16.

Data Availability

The data that support the findings of this study are available within the paper and its Supplementary Information.

Competing interests

The Authors declare no conflict of interests.

Acknowledgments

RFLE gratefully acknowledges the financial support of ARCHER UK National Supercomputing Service via the embedded CSE programme (ecse1307). EJGS acknowledges computational resources through the UK Materials and Molecular Modelling Hub for access to THOMAS supercluster, which is partially funded by EPSRC (EP/P020194/1); CIRRUS Tier-2 HPC Service (ec131 Cirrus Project) at EPCC (http://www.cirrus.ac.uk) funded by the University of Edinburgh and EPSRC (EP/P020267/1); ARCHER UK National Supercomputing Service (http://www.archer.ac.uk) via Project d429. EJGS acknowledges the EPSRC Early Career Fellowship (EP/T021578/1) and the University of Edinburgh for funding support.

Author Contributions

EJGS conceived the idea and supervised the project. IMA performed ab initio and Monte Carlo simulations under the supervision of EJGS. IMA and EJGS elaborated the analysis and figures. RFLE implemented the spin-transfer-torque method. EJGS wrote the paper with inputs from all authors. KSN helped in the analysis and discussions. All authors contributed to this work, read the manuscript, discussed the results, and agreed to the contents of the manuscript.

References and Notes

1. Huang, B. *et al.* Layer-dependent ferromagnetism in a van der waals crystal down to the monolayer limit. *Nature* **546**, 270 EP – (2017). URL https://doi.org/10.1038/nature22391.

2. Gong, C. *et al.* Discovery of intrinsic ferromagnetism in two-dimensional van der waals crystals. *Nature* **546**, 265–269 (2017). URL http://dx.doi.org/10.1038/nature22060. Letter.

3. Guguchia, Z. *et al.* Magnetism in semiconducting molybdenum dichalcogenides. *Science Advances* **4** (2018). URL https://advances.sciencemag.org/content/4/12/eaat3672. https://advances.sciencemag.org/content/4/12/eaat3672.full.pdf.

4. Klein, D. R. *et al.* Probing magnetism in 2d van der waals crystalline insulators via electron tunneling. *Science* **360**, 1218–1222 (2018). URL http://

science.sciencemag.org/content/360/6394/1218. http://science.sciencemag.org/content/360/6394/1218.full.pdf.

5. Gibertini, M., Koperski, M., Morpurgo, A. F. & Novoselov, K. S. Magnetic 2d materials and heterostructures. *Nature Nanotechnology* **14**, 408–419 (2019). URL https://doi.org/10.1038/s41565-019-0438-6.

6. Gong, C. & Zhang, X. Two-dimensional magnetic crystals and emergent heterostructure devices. *Science* **363** (2019). URL https://science.sciencemag.org/content/363/6428/eaav4450. https://science.sciencemag.org/content/363/6428/eaav4450.full.pdf.

7. Li, L. H., Tian, T., Cai, Q., Shih, C.-J. & Santos, E. J. G. Asymmetric electric field screening in van der waals heterostructures. *Nature Communications* **9**, 1271 (2018). URL https://doi.org/10.1038/s41467-018-03592-3.

8. Santos, E. J. G. Carrier-mediated magnetoelectric coupling in functionalized graphene. *ACS Nano* **7**, 9927–9932 (2013). URL https://doi.org/10.1021/nn4037877.

9. Hong, J. *et al.* Intrinsic controllable magnetism of graphene grown on fe. *The Journal of Physical Chemistry C* **123**, 26870–26876 (2019). URL https://doi.org/10.1021/acs.jpcc.9b05886.

10. Tian, T. *et al.* Electronic polarizability as the fundamental variable in the dielectric properties of two-dimensional materials. *Nano Letters* **20**, 841–851 (2020). URL https://doi.org/10.1021/acs.nanolett.9b02982.

11. Okuda, K. *et al.* Magnetic properties of layered compound mnps3. *Journal of the Physical Society of Japan* **55**, 4456–4463 (1986). URL https://doi.org/10.1143/JPSJ.55.4456. https://doi.org/10.1143/JPSJ.55.4456.

12. Makimura, C., Sekine, T., Tanokura, Y. & Kurosawa, K. Raman scattering in the two-dimensional antiferromagnet MnPSe3. *Journal of Physics: Condensed Matter* **5**, 623–632 (1993). URL https://doi.org/10.1088%2F0953-8984%2F5%2F5%2F013.

13. Baltz, V. *et al.* Antiferromagnetic spintronics. *Rev. Mod. Phys.* **90**, 015005 (2018). URL https://link.aps.org/doi/10.1103/RevModPhys.90.015005.

14. Long, G. *et al.* Isolation and characterization of few-layer manganese thiophosphite. *ACS Nano* **11**, 11330–11336 (2017). URL https://doi.org/10.1021/acsnano.7b05856.

15. Kim, K. *et al.* Antiferromagnetic ordering in van der waals 2d magnetic material MnPS3 probed by raman spectroscopy. *2D Materials* **6**, 041001 (2019). URL https://doi.org/10.1088%2F2053-1583%2Fab27d5.

16. Song, T. *et al.* Giant tunneling magnetoresistance in spin-filter van der waals heterostructures. *Science* **360**, 1214–1218 (2018). URL http://science.sciencemag.org/content/360/6394/1214. http://science.sciencemag.org/content/360/6394/1214.full.pdf.

17. Wang, Z. *et al.* Very large tunneling magnetoresistance in layered magnetic semiconductor CrI3. *Nat. Commun.* **9**, 2516 (2018).

18. Song, T. *et al.* Switching 2d magnetic states via pressure tuning of layer stacking. *Nature Materials* **18**, 1298–1302 (2019). URL https://doi.org/10.1038/s41563-019-0505-2.

19. Chen, W. *et al.* Direct observation of van der waals stacking–dependent interlayer magnetism. *Science* **366**, 983–987 (2019). URL https://science.sciencemag.org/content/366/6468/983. https://science.sciencemag.org/content/366/6468/983.full.pdf.

20. Thiel, L. *et al.* Probing magnetism in 2d materials at the nanoscale with single-spin microscopy. *Science* (2019). URL https://science.sciencemag.org/content/early/2019/04/24/science.aav6926. https://science.sciencemag.org/content/early/2019/04/24/science.aav6926.full.pdf.

21. Zhong, D. *et al.* Layer-resolved magnetic proximity effect in van der waals heterostructures. *Nature Nanotechnology* **15**, 187–191 (2020). URL https://doi.org/10.1038/s41565-019-0629-1.

22. Wahab, D. A. *et al.* Quantum rescaling, metastability and hybrid domain-walls in two-dimensional cri_3 magnets. *arXiv:* (2020).

23. Long, G. *et al.* Persistence of magnetism in atomically thin mnps3 crystals. *Nano Letters* **20**, 2452–2459 (2020). URL https://doi.org/10.1021/acs.nanolett.9b05165.

24. Hubert, A. & Schafer, R. *Magnetic Domains: The Analysis of Magnetic Microstructures* (Springer Science and Business Media, 2008).

25. Schlickum, U., Janke-Gilman, N., Wulfhekel, W. & Kirschner, J. Step-induced frustration of antiferromagnetic order in mn on fe(001). *Phys. Rev. Lett.* **92**, 107203 (2004). URL https://link.aps.org/doi/10.1103/PhysRevLett.92.107203.

26. Jungwirth, T., Marti, X., Wadley, P. & Wunderlich, J. Antiferromagnetic spintronics. *Nature Nanotechnology* **11**, 231–241 (2016). URL https://doi.org/10.1038/nnano.2016.18.

27. Shiino, T. *et al.* Antiferromagnetic domain wall motion driven by spin-orbit torques. *Phys. Rev. Lett.* **117**, 087203 (2016). URL https://link.aps.org/doi/10.1103/PhysRevLett.117.087203.

28. Haldane, F. D. M. Nonlinear field theory of large-spin heisenberg antiferromagnets: Semi-classically quantized solitons of the one-dimensional easy-axis néel state. *Phys. Rev. Lett.* **50**, 1153–1156 (1983). URL https://link.aps.org/doi/10.1103/PhysRevLett.50.1153.

29. Kim, S. K., Tserkovnyak, Y. & Tchernyshyov, O. Propulsion of a domain wall in an antiferromagnet by magnons. *Phys. Rev. B* **90**, 104406 (2014). URL https://link.aps.org/doi/10.1103/PhysRevB.90.104406.

30. Oguchi, T. Theory of spin-wave interactions in ferro- and antiferromagnetism. *Phys. Rev.* **117**, 117–123 (1960). URL https://link.aps.org/doi/10.1103/PhysRev.117.117.

31. Kubo, R. The spin-wave theory of antiferromagnetics. *Phys. Rev.* **87**, 568–580 (1952). URL https://link.aps.org/doi/10.1103/PhysRev.87.568.

32. Wieser, R., Vedmedenko, E. Y. & Wiesendanger, R. Domain wall motion damped by the emission of spin waves. *Phys. Rev. B* **81**, 024405 (2010). URL https://link.aps.org/doi/10.1103/PhysRevB.81.024405.

33. Bouzidi, D. & Suhl, H. Motion of a bloch domain wall. *Phys. Rev. Lett.* **65**, 2587–2590 (1990). URL https://link.aps.org/doi/10.1103/PhysRevLett.65.2587.

345 34. Tveten, E. G., Qaiumzadeh, A. & Brataas, A. Antiferromagnetic domain wall motion induced
346 by spin waves. *Phys. Rev. Lett.* **112**, 147204 (2014). URL https://link.aps.org/doi/
347 10.1103/PhysRevLett.112.147204.

348 35. Nishitani, J., Nagashima, T. & Hangyo, M. Terahertz radiation from antiferromagnetic mno
349 excited by optical laser pulses. *Applied Physics Letters* **103**, 081907 (2013). URL https:
350 //doi.org/10.1063/1.4819181.

351 36. Kampfrath, T. *et al.* Coherent terahertz control of antiferromagnetic spin waves. *Nature*
352 *Photonics* **5**, 31–34 (2011). URL https://doi.org/10.1038/nphoton.2010.259.

353 37. Satoh, T. *et al.* Spin oscillations in antiferromagnetic nio triggered by circularly polarized
354 light. *Phys. Rev. Lett.* **105**, 077402 (2010). URL https://link.aps.org/doi/10.1103/
355 PhysRevLett.105.077402.

356 38. Kimel, A. V. *et al.* Ultrafast non-thermal control of magnetization by instantaneous photomag-
357 netic pulses. *Nature* **435**, 655–657 (2005). URL https://doi.org/10.1038/nature03564.

358 39. Mukai, Y., Hirori, H., Yamamoto, T., Kageyama, H. & Tanaka, K. Antiferromagnetic res-
359 onance excitation by terahertz magnetic field resonantly enhanced with split ring resonator.
360 *Applied Physics Letters* **105**, 022410 (2014). URL https://doi.org/10.1063/1.4890475.

361 40. Vaidya, P. *et al.* Subterahertz spin pumping from an insulating antiferromagnet. *Sci-*
362 *ence* **368**, 160 (2020). URL http://science.sciencemag.org/content/368/6487/160.
363 abstract.

41. Nikitenko, V. I. *et al.* Asymmetry in elementary events of magnetization reversal in a ferromagnetic/antiferromagnetic bilayer. *Phys. Rev. Lett.* **84**, 765–768 (2000). URL https://link.aps.org/doi/10.1103/PhysRevLett.84.765.

42. Nakatani, Y., Thiaville, A. & Miltat, J. Faster magnetic walls in rough wires. *Nature Materials* **2**, 521–523 (2003). URL https://doi.org/10.1038/nmat931.

43. Kartsev, A. *et al.* Higher-order exchange interactions in two-dimensional magnets. *arXiv:* (2020).

Figure captions

Figure 1: **Magnetic domain evolution of a 2D antiferromagnet.** Snapshots of the dynamic spin configuration of monolayer $MnPS_3$ during field-cooling at different temperatures (K), time steps (ns) and different magnetic fields: **a-e,** 0 T and **f-j** 0.2 T. The out-of-plane component of the magnetization S_z is used to follow the evolution in a 0.3 μm$\times$ 0.3 μm square flake. Labels on temperatures and time are the same for both magnitudes of the field at the same column. Color scale in **e** shows the variation of S_z. To provide a better visualization of the domains we inverted the colour scheme for the two sublattices. That is, spin up (spin down) corresponds to red (blue) for one of the sublattices, and blue (red) for the other. This convention results in a single colour for a given domain. See Supplementary Note 8 for further details.

Figure 2: **Hybrid domain wall formation and spin rotation. a-b,** Local and global view, respectively, of a snapshot of one of the spin configurations in a 300 nm $\times$ 50 nm ribbon of $MnPS_3$. The small rectangle in **b** corresponds to area studied in **a**. The out-of-plane component of the magnetization S_z(color map) is utilized to monitor the formation of the domain wall. Spins rotated across the wall in pairs forming an angle ϕ with the zig-zag crystallographic direction of the honeycomb lattice of 64.02^{o}. The system is at zero magnetic field and 0 K. **c-d,** Profile of the magnetization along the domain wall projected along S_z and the in-plane (S_x, S_y) components, respectively. Fitting curves are obtained using Eqs. $1-2$. We computed domain wall widths $\sigma_z = 3.41$ nm (± 0.03) and $\sigma_x, y = 3.50$ nm (± 0.06). **e-f,** Top and side views, respectively, of the rotation of the magnetization along the domain wall. Both S_x and S_y show variations along the wall altogether with S_z which indicate a hybrid character of the domain wall, i.e. neither Bloch nor Néel. Colours follow the scale bar in **b**.

Figure 3: **Field- and current-induced domain wall dynamics in a 2D antiferromagnet a,** Snapshots of the domain wall dynamics in $MnPS_3$ induced by electric currents $j(10^9$ A cm$^{-2})$ and magnetic fields B(T). The initial domain wall configuration (j=0, B=0) is the same for both driving forces at t=0 ns (middle panel). The current-driven domain wall motion is shown at different current densities ($2\times10^8-5\times10^{10}$ A cm^{-2}) but at the same time evolution of 0.5 ns (upper panels). For the field-induced domain wall motion (lower panels), two magnitudes at 2 T and 4 T are shown. A 300 nm$\times$50 nm flake is considered in all simulations. **b,** Simulated wall velocity v (m s^{-1}) versus current density j (10^9 A cm^{-2}) (triangles) considering two fits to the data. In the low-velocity regime, Eq.3 is used to describe the linear dependence (black curve). In the relativistic regime, Eq.4 provides an accurate description over the entire range of densities. Maximum group velocities v_{g1} and v_{g2} are shown for comparison via horizontal dashed lines in the coloured region. **c,** Variation of the out-of-plane component of the magnetization S_z across the domain wall with a current density of 2×10^9 A cm^{-2} at t=0.0, 0.25, 0.5 ns. The calculated points are fitted to Eq.2 shown with the solid line. The variation in position of the centre of the domain wall as a function of time is used to extract the wall velocity which is an average over all atoms at the domain wall. **d-e,** Current-driven domain wall width σ (nm) and domain wall mass $M_{\rm DW}$, respectively, versus v. Fits to Eq. 5 and Eq. 6 are included for comparison. **f-g,** In-plane components of the magnetization $S_{x,y}$ (a.u.) versus time (ps), respectively, for $j=2\times10^9$ A cm^{-2}. Frequencies within the range of $0.79-0.81$ THz can be extracted from $S_{x,y}$ shown via the solid curves in a full circle. **h,** Close look of the snapshot of the field-induced domain wall motion at B=2.0 T in **a**. The presence of different edges (zigzag and dangling-bond) terminating the layer along y induces a bending of the wall profile under the field and consequently a slight asymmetry in the displacement of the wall. Only Mn atoms in the honeycomb lattice are shown. **i,** Wall velocity versus magnetic field applied perpendicular to the surface. The dashed line is given by $y=86.28x$ with linear regression coefficient $R^2=0.9996$. **j,** Similar as **c** but at an applied field of 2.0 T. The initial condition shows that the spin directions of all atoms at the same x (and any y) appear superimposed on top of each other, revealing a highly ordered system. As the wall motion starts, atoms at the same x but different y no longer have the same spin direction, leading to a continuous distribution of spins.

Figure 4: **Sublattice mediated domain-wall motion in a 2D anti-ferromagnet under magnetic fields. a,** Schematic of the intended wall motion taking place in opposite directions at different sublattices (i.e. A or B) under an external field B_z. Only atoms at one sublattice (green or violet) are shown around each edge to facilitate the view. The rotation of the spins over time at sublattices A (green) and B (violet) are represented with the arrows changing systematically in the background. Only Mn atoms are shown. **b-c,** Monolayer $MnPS_3$ terminated with both edges in zig-zag (ZZ) configuration, and with a combination of ZZ and dangling-bond (DB) arrangements, respectively. The domain wall is shown at the faint atoms in the middle of the layer. **d,** Diagram of the energy versus the angle θ defined relative to the z-axis. Away from the domain wall, θ can be either 0^o or 180^o depending on what sublattice is considered. At the wall, θ can range within $0-180^o$ for one sublattice, and $180-0^o$ for the other. B_z points along of $z<0$. Spins at the wall ($0^o<\theta<180^o$, which excludes fully spin-up and spin-down states) react differently than those away from the wall (i.e., $\theta=0$ for spin-up or $theta=180^o$ for spin down) to an external magnetic field. Only for those at the wall, a finite B_z changes the energetic stability of the system inducing a rotation of the spins as the magnitude of θ changes to a new energy minimum (e.g. $\theta_{B_z=0}\neq\theta_{B_z\neq0}$). ΔE shows the energy gained through a rotation to the new minimum once the field is applied. For the spins away from the wall, B_z causes a rigid shift of the energy curve while preserving its shape. This results in no change in the value of θ for the minimum energy, and thus, no rotation induced locally by the magnetic field. The energy is calculated via Eq. 8. **e-f,** Plots of $-\Delta$E for few atoms at different regions of the layer such as at the edges, near the edges and middle of the sheet for systems with ZZ-ZZ and ZZ-DB edges, respectively. The different sublattices (A and B) are shown individually in different coloured curves. We plot $-\Delta$E instead of ΔE to better display the variations of energy at different parts of the system. The inset in **f** shows a side view of the layer with the dimensions considered in the model.

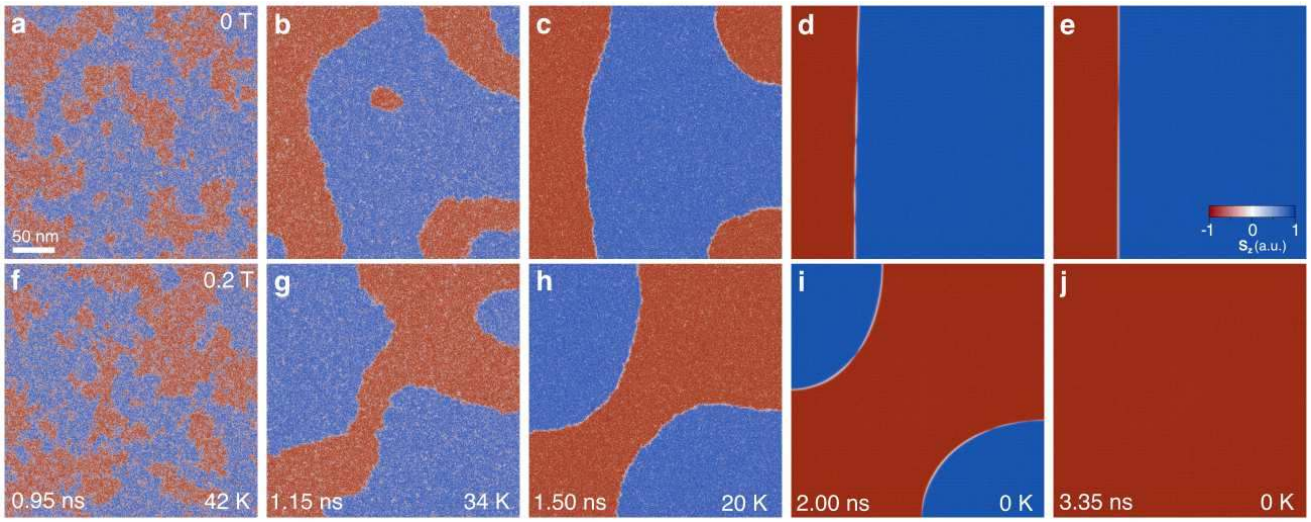
a
0 T
50 nm
b
c
d
e
-1
0
1
S_z(a.u.)
f
0.2 T
0.95 ns
42 K
g
1.15 ns
34 K
h
1.50 ns
20 K
i
2.00 ns
0 K
j
3.35 ns
0 K

Figure 1

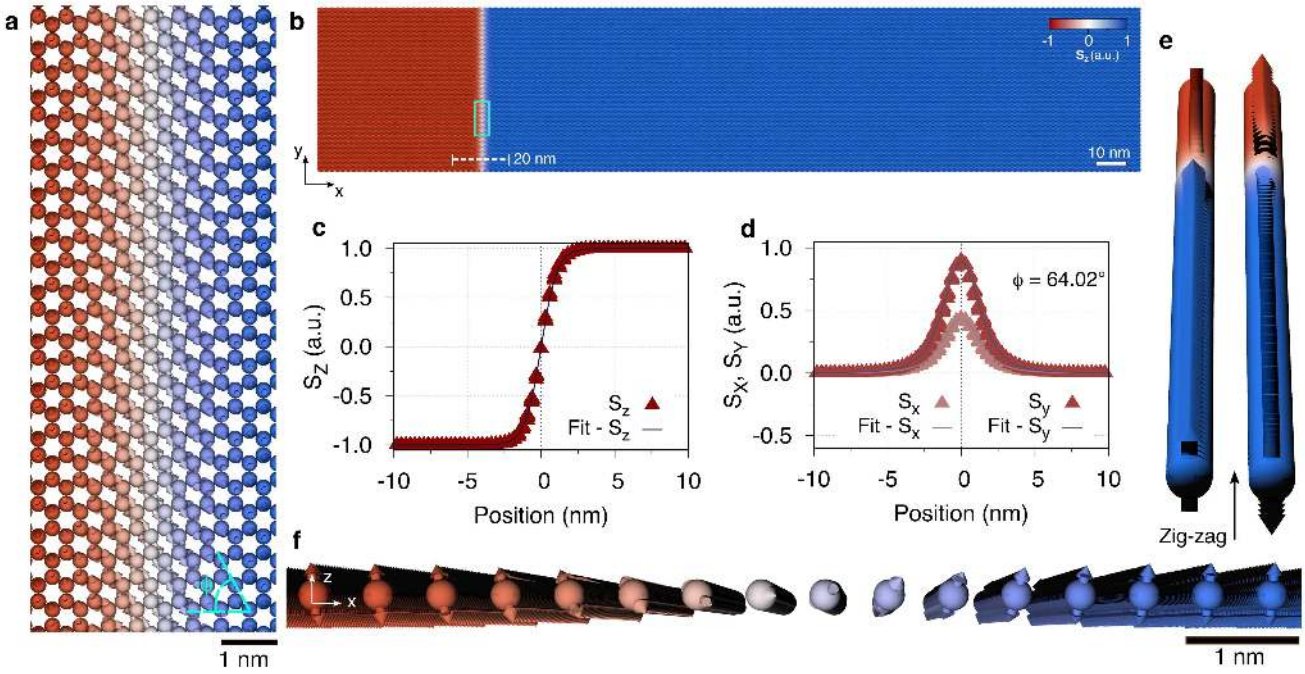
a
b
-1 0 1
S_z (a.u.)
20 nm
10 nm
y
x
c
1.0
0.5
0.0
-0.5
-1.0
S_Z (a.u.)
S_z
Fit - S_z
-10 -5 0 5 10
Position (nm)
d
1.0
0.5
0.0
-0.5
S_X, S_Y (a.u.)
ϕ = 64.02°
S_x
Fit - S_x
S_y
Fit - S_y
-10 -5 0 5 10
Position (nm)
e
Zig-zag
f
z
x
1 nm
1 nm

Figure 2

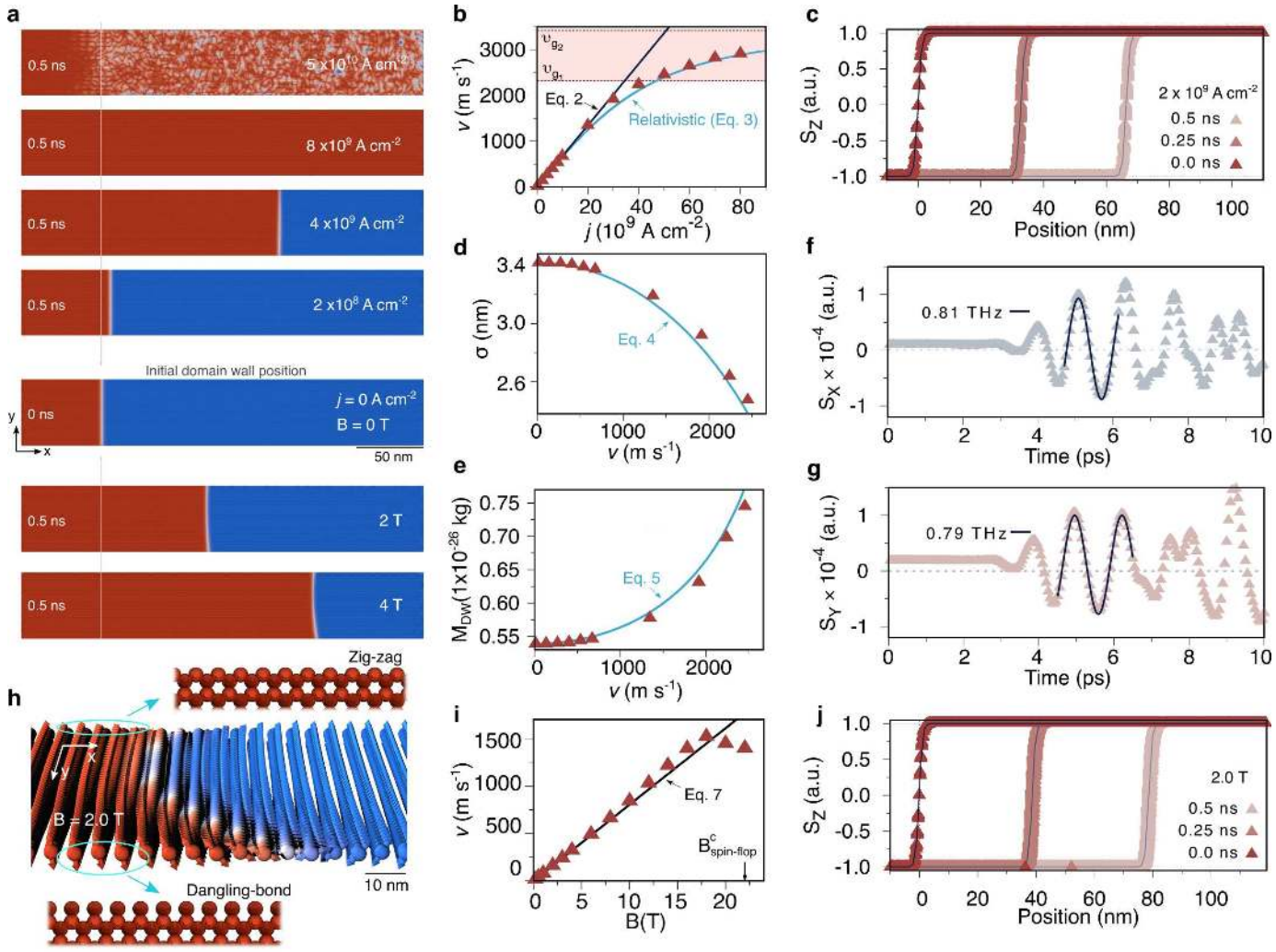
a
0.5 ns
5 x10^10 A cm^-2
0.5 ns
8 x10^9 A cm^-2
0.5 ns
4 x10^9 A cm^-2
0.5 ns
2 x10^9 A cm^-2
Initial domain wall position
0 ns
j = 0 A cm^-2
B = 0 T
50 nm
y
x
0.5 ns
2 T
0.5 ns
4 T
b
v (m s^-1)
Eq. 2
Relativistic (Eq. 3)
j (10^9 A cm^-2)
c
S_Z (a.u.)
2 x 10^9 A cm^-2
0.5 ns
0.25 ns
0.0 ns
Position (nm)
d
σ (nm)
Eq. 4
v (m s^-1)
f
S_X x 10^-4 (a.u.)
0.81 THz
Time (ps)
e
M_DW(1x10^-26 kg)
Eq. 5
v (m s^-1)
g
S_Y x 10^-4 (a.u.)
0.79 THz
Time (ps)
h
Zig-zag
B = 2.0 T
Dangling-bond
10 nm
i
v (m s^-1)
Eq. 7
B^c_spin-flop
B(T)
j
S_Z (a.u.)
2.0 T
0.5 ns
0.25 ns
0.0 ns
Position (nm)

Figure 3

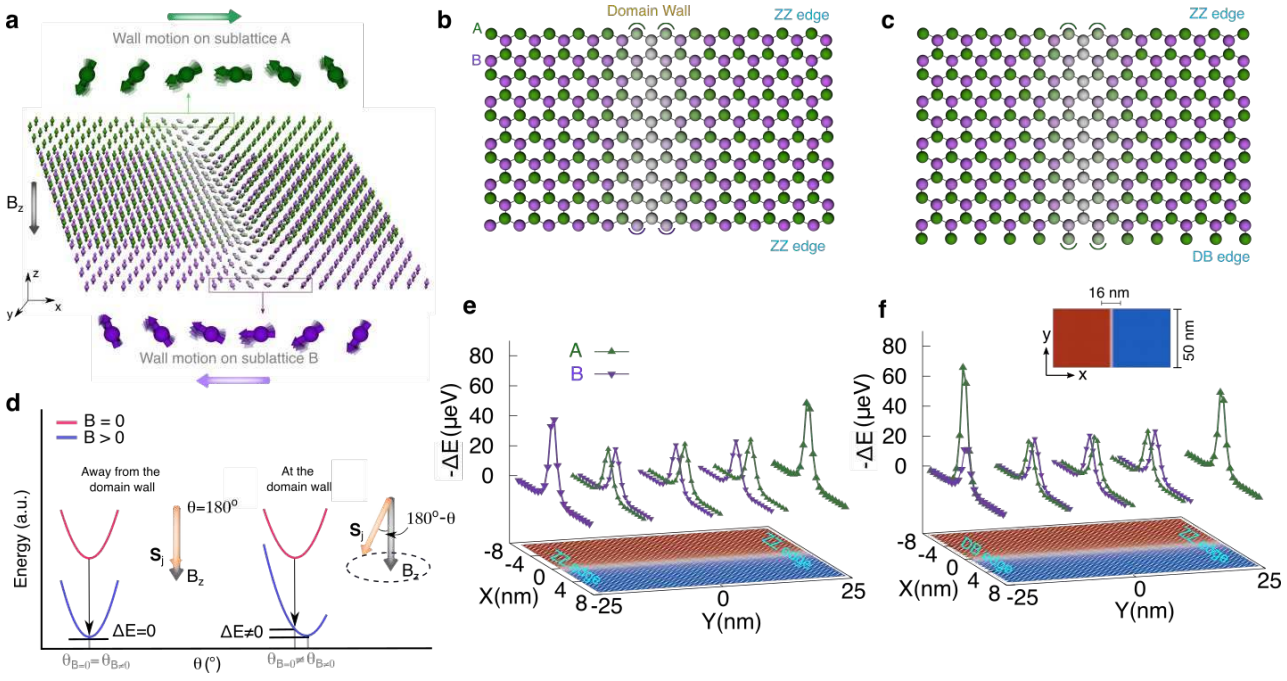
a
Wall motion on sublattice A
Wall motion on sublattice B
B_z
z
x
y
b
Domain Wall
ZZ edge
A
B
ZZ edge
c
ZZ edge
DB edge
d
B = 0
B > 0
Away from the domain wall
At the domain wall
θ=180°
180°-θ
S_j
B_z
ΔE=0
ΔE≠0
Energy (a.u.)
θ (°)
e
A
B
-ΔE (μeV)
X(nm)
Y(nm)
f
16 nm
50 nm
y
x
-ΔE (μeV)
X(nm)
Y(nm)

Figures

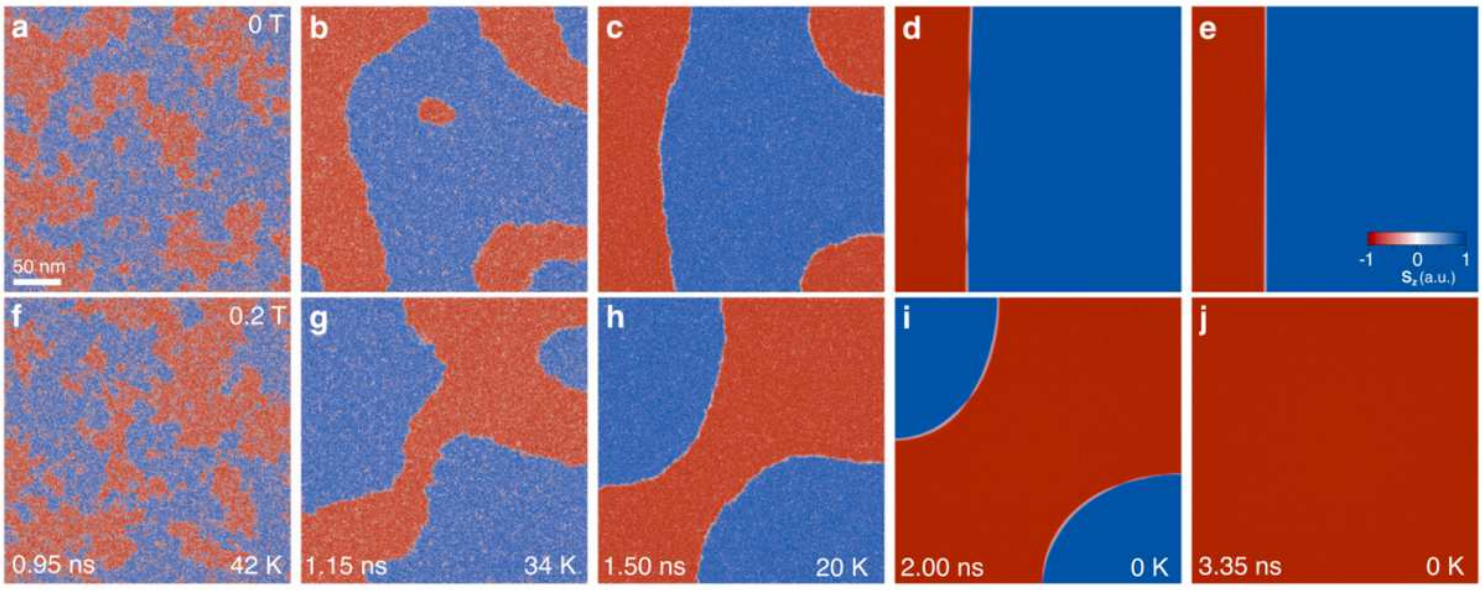

Figure 1

Magnetic domain evolution of a 2D antiferromagnet. Snapshots of the dynamic spin configuration of monolayer MnPS3 during field-cooling at different temperatures (K), time steps (ns) and different magnetic fields: a-e, 0 T and f-j 0.2 T. The out-of-plane component of the magnetization Sz is used to follow the evolution in a 0.3 μm× 0.3 μm square flake. Labels on temperatures and time are the same for both magnitudes of the field at the same column. Color scale in e shows the variation of Sz. To provide a better visualization of the domains we inverted the colour scheme for the two sublattices. That is, spin up (spin down) corresponds to red (blue) for one of the sublattices, and blue (red) for the other. This convention results in a single colour for a given domain. See Supplementary Note 8 for further details.

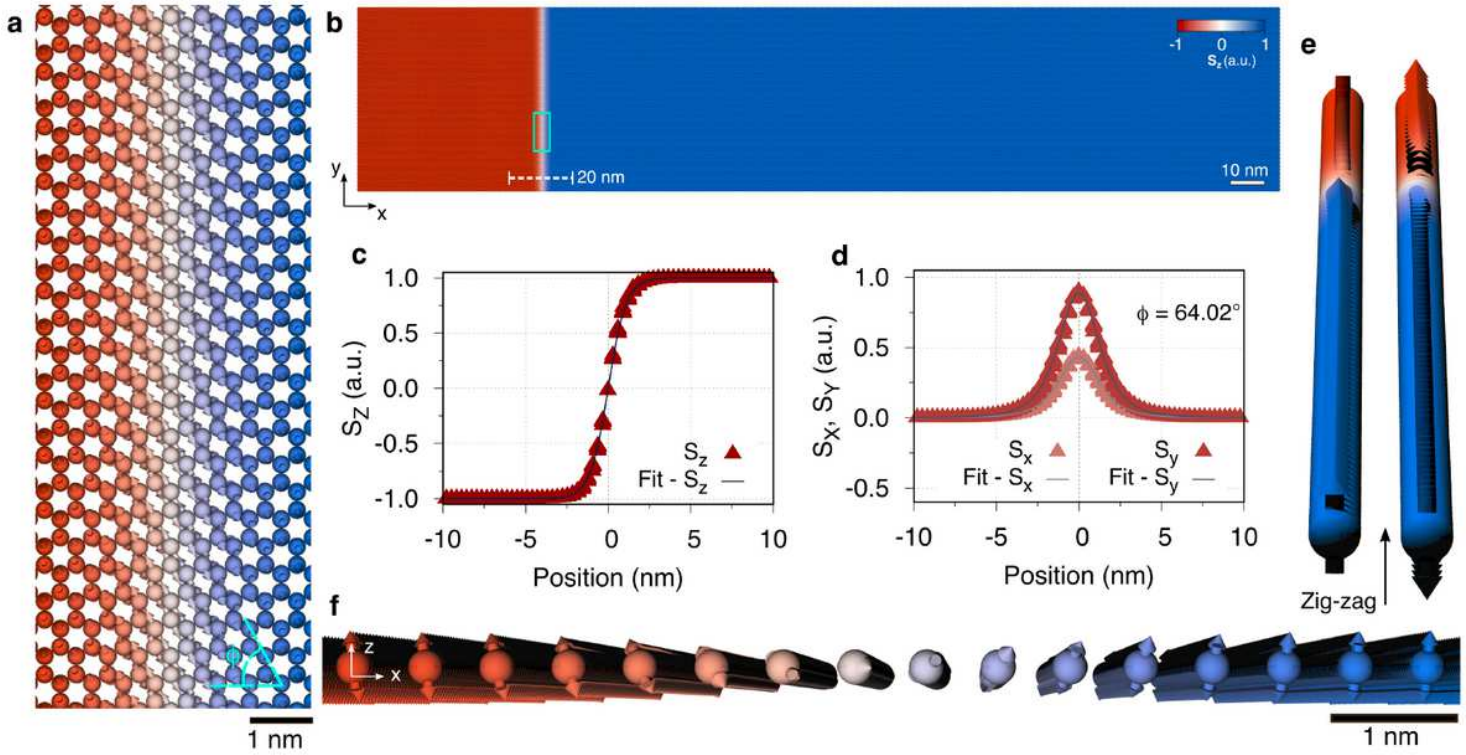

Figure 2

Hybrid domain wall formation and spin rotation. a-b, Local and global view, respectively, of a snapshot of one of the spin configurations in a 300 nm × 50 nm ribbon of MnPS3. The small rectangle in b corresponds to area studied in a. The out-of-plane component of the magnetization Sz(color map) is utilized to monitor the formation of the domain wall. Spins rotated across the wall in pairs forming an angle φ with the zig-zag crystallographic direction of the honeycomb lattice of 64.02o. The system is at zero magnetic field and 0 K. c-d, Profile of the magnetization along the domain wall projected along Sz and the in-plane (Sx, Sy) components, respectively. Fitting curves are obtained using Eqs. 1–2. We computed domain wall widths σz = 3.41 nm (±0.03) and σx,y = 3.50 nm (±0.06). e-f, Top and side views, respectively, of the rotation of the magnetization along the domain wall. Both Sx and Sy show variations along the wall altogether with Sz which indicate a hybrid character of the domain wall, i.e. neither Bloch nor N´eel. Colours follow the scale bar in b.

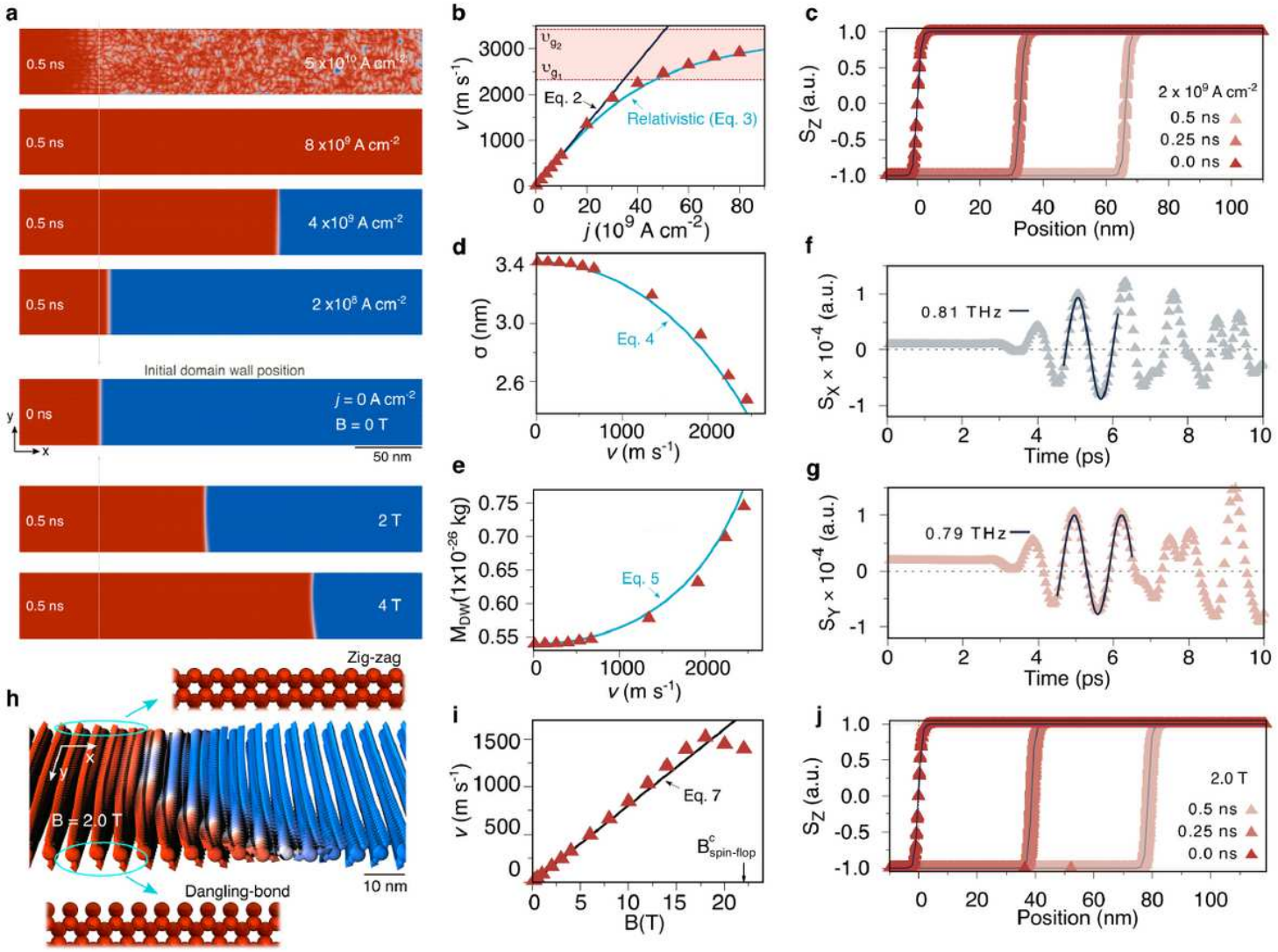

Figure 3

Field- and current-induced domain wall dynamics in a 2D antiferromagnet a, Snapshots of the domain wall dynamics in MnPS3 induced by electric currents j(109 A cm−2) and magnetic fields B(T). The initial domain wall configuration (j=0, B=0) is the same for both driving forces at t=0 ns (middle panel). The current-driven domain wall motion is shown at different current densities (2 × 108 − 5 × 1010 A cm−2) but at the same time evolution of 0.5 ns (upper panels). For the field-induced domain wall motion (lower panels), two magnitudes at 2 T and 4 T are shown. A 300 nm×50 nm flake is considered in all simulations. b, Simulated wall velocity v (m s−1) versus current density j (109 A cm−2) (triangles) considering two fits to the data. In the low-velocity regime, Eq.3 is used to describe the linear dependence (black curve). In the relativistic regime, Eq.4 provides an accurate description over the entire range of densities. Maximum group velocities vg1 and vg2 are shown for comparison via horizontal dashed lines in the coloured region. c, Variation of the out-of-plane component of the magnetization Sz across the domain wall with a current density of 2 ×109 A cm−2 at t=0.0, 0.25, 0.5 ns. The calculated points are fitted to Eq.2 shown with the solid line. The variation in position of the centre of the domain wall as a function of time is used to extract the wall velocity which is an average over all atoms at the domain wall.

d-e, Current-driven domain wall width σ (nm) and domain wall mass MDW, respectively, versus v. Fits to Eq. 5 and Eq. 6 are included for comparison. f-g, In-plane components of the magnetization Sx,y (a.u.) versus time (ps), respectively, for j = 2 × 109 A cm−2. Frequencies within the range of 0.79–0.81 THz can be extracted from Sx,y shown via the solid curves in a full circle. h, Close look of the snapshot of the field-induced domain wall motion at B=2.0 T in a. The presence of different edges (zigzag and dangling-bond) terminating the layer along y induces a bending of the wall profile under the field and consequently a slight asymmetry in the displacement of the wall. Only Mn atoms in the honeycomb lattice are shown. i, Wall velocity versus magnetic field applied perpendicular to the surface. The dashed line is given by y = 86.28x with linear regression coefficient R2 = 0.9996. j, Similar as c but at an applied field of 2.0 T. The initial condition shows that the spin directions of all atoms at the same x (and any y) appear superimposed on top of each other, revealing a highly ordered system. As the wall motion starts, atoms at the same x but different y no longer have the same spin direction, leading to a continuous distribution of spins.

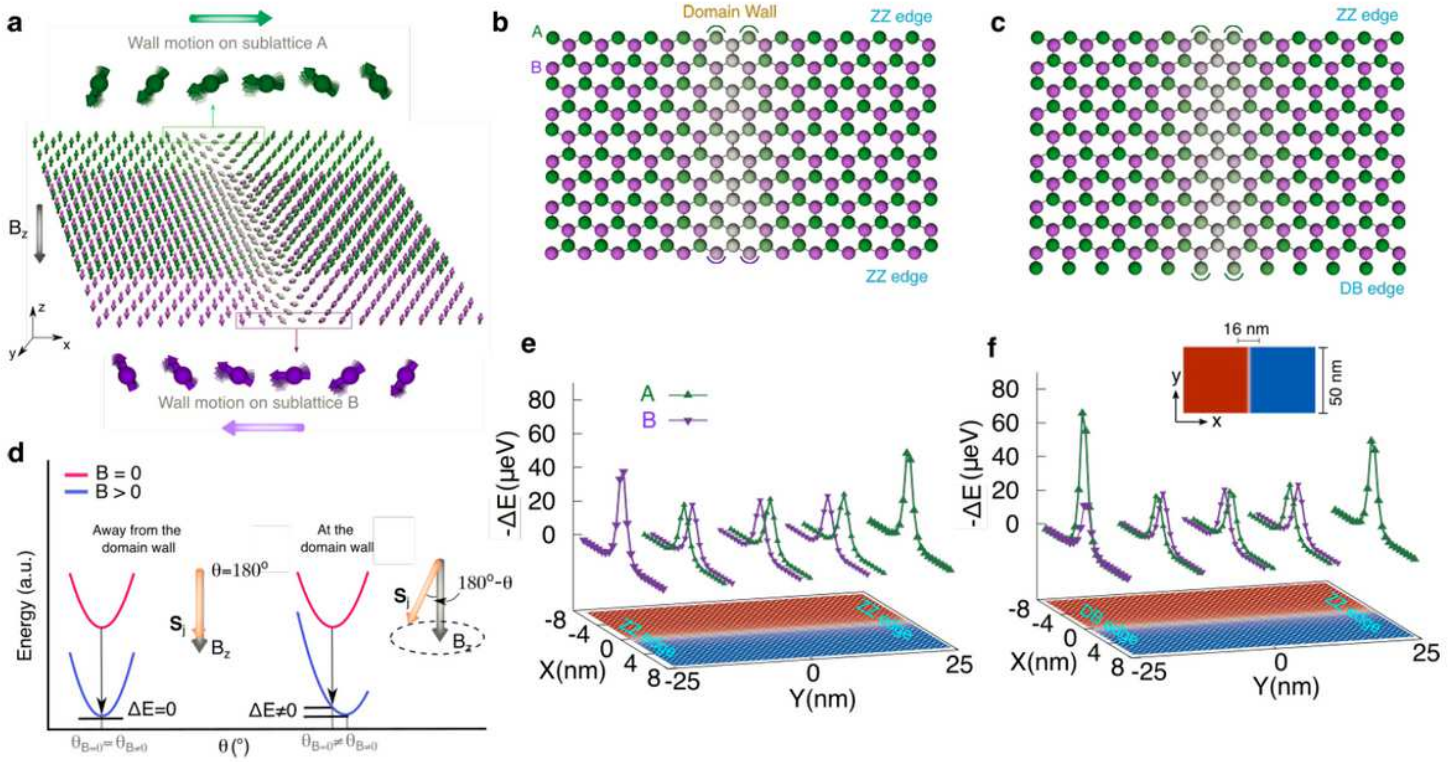

Figure 4

Sublattice mediated domain-wall motion in a 2D anti-ferromagnet under magnetic fields. a, Schematic of the intended wall motion taking place in opposite directions at different sublattices (i.e. A or B) under an external field Bz. Only atoms at one sublattice (green or violet) are shown around each edge to facilitate the view. The rotation of the spins over time at sublattices A (green) and B (violet) are represented with the arrows changing systematically in the background. Only Mn atoms are shown. b-c, Monolayer MnPS3 terminated with both edges in zig-zag (ZZ) configuration, and with a combination of ZZ and dangling-bond (DB) arrangements, respectively. The domain wall is shown at the faint atoms in the middle of the layer. d, Diagram of the energy versus the angle θ defined relative to the z-axis. Away from the domain

wall, θ can be either 0o or 180o depending on what sublattice is considered. At the wall, θ can range within 0 − 180o for one sublattice, and 180 − 0o for the other. Bz points along of z < 0. Spins at the wall (0o < θ < 180o, which excludes fully spin-up and spin-down states) react differently than those away from the wall (i.e., θ = 0 for spin-up or theta = 180o for spin down) to an external magnetic field. Only for those at the wall, a finite Bz changes the energetic stability of the system inducing a rotation of the spins as the magnitude of θ changes to a new energy minimum (e.g. θBz=0 = θBz=0). ΔE shows the energy gained through a rotation to the new minimum once the field is applied. For the spins away from the wall, Bz causes a rigid shift of the energy curve while preserving its shape. This results in no change in the value of θ for the minimum energy, and thus, no rotation induced locally by the magnetic field. The energy is calculated via Eq. 8. e-f, Plots of −ΔE for few atoms at different regions of the layer such as at the edges, near the edges and middle of the sheet for systems with ZZ-ZZ and ZZ-DB edges, respectively. The different sublattices (A and B) are shown individually in different coloured curves. We plot −ΔE instead of ΔE to better display the variations of energy at different parts of the system. The inset in f shows a side view of the layer with the dimensions considered in the model.

Supplementary Files

This is a list of supplementary files associated with this preprint. Click to download.

- SIMnPS3domainv092920.pdf